A Platform for Nuclear Physics Experiments with Laser-Accelerated Light Ions

Introduction

Powerful laser facilities that have become operational over the past few years have the potential to expand research opportunities in several fields of scientific research.[1] Nuclear science (physics and chemistry) could play a key role in the development of the emerging field of high-energy-density laboratory physics (HEDLP). The role of nuclear science includes the development of nuclear detectors for detailed plasma diagnostics and novel methods for the study of basic and applied nuclear science specific to the laser-driven plasma environment. Laser-driven experiments have studied aspects of nuclear science and applications using both long-pulse (nanosecond)–driven implosions, which generate neutrons from thermonuclear reactions,[2,3] and short-pulse (picosecond) laser–plasma interactions, which accelerate ions to energies high enough for nuclear reactions.[4,5]

The proposed experimental platform produces light-ion beams of controllable intensity, energy, and spatial collimation. It is based on the principle of the laser-induced acceleration process known as target normal sheath acceleration (TNSA).[6]

Figure 156.13 illustrates this process in which enormous Coulomb fields (~GV/m) are generated suddenly (within picoseconds) on the back side of a primary "converter" foil irradiated with high-power, short-pulse laser beams. Relativistic electrons generated in the laser–target interaction escape the target, leaving behind ions and therefore generating a large sheath field E_z, especially at the back side of the target. Particles (open circles in Fig. 156.13) either adsorbed to the back surface or from a thin layer of the target are ionized by the passing electrons and the high electric field and are accelerated to high energies (~MeV) toward a secondary target, in which they induce nuclear reactions.

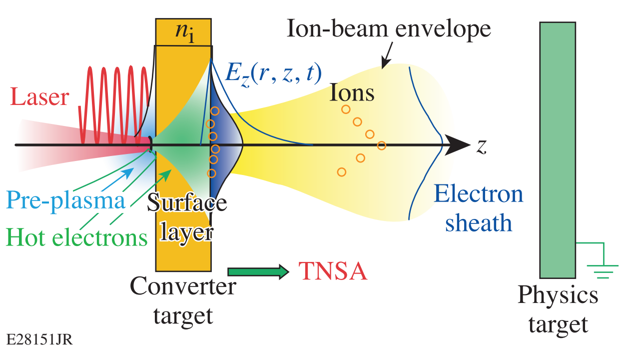

Figure 156.13
Target normal sheath acceleration (TNSA) process: Laser beams from the left force a sheath of electrons to separate from the back side of a metallic converter foil. The resulting coulomb field accelerates ions (here tritons) in the near-surface domain of foil. A beam of ions is accelerated toward the physics target to be studied. Modified after Ref. 7.

Figure 156.14 shows a schematic of the experimental setup of the nuclear physics experiments on OMEGA EP. The ions are generated from the laser-irradiated converter target through the TNSA process. The ion beam strikes a secondary (physics) target and produces neutrons through nuclear reactions. The number of neutrons is inferred from nuclear activation detectors, and the neutron energy spectrum is recorded on neutron time-of-flight (nTOF) detectors placed in different directions with respect to the laser axis to estimate the angular distribu-

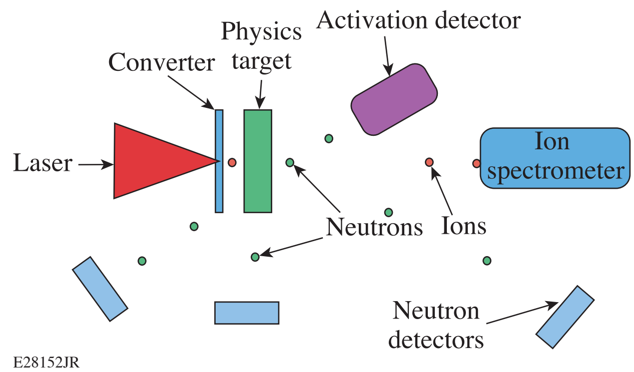

Figure 156.14
Schematic of the experimental setup (not to scale). The laser beam is focused on the converter target and generates fast ions. The ion-energy spectrum can be measured by an ion detector by removing the secondary target. Neutrons produced in a nuclear reaction in the secondary target are detected by nuclear activation detectors and neutron detectors mounted in different directions relative to the laser axis.

tion of the neutrons. By removing the physics target, the energy spectrum of the ion beam can be directly measured using an ion spectrometer. The angular distribution of the ion beam can be inferred with an ion-sensitive film, which is fielded in place of the ion spectrometer on a separate experiment.

Laser-based neutron sources are also an interesting alternative to conventional neutron sources like reactors and spallation sources for many applications in science and engineering. Potential applications include radiography of cargo containers for homeland security,[8] temperature measurement of opaque materials,[9] boron neutron capture therapy in cancer treatment,[10] and damage studies of potential fusion chamber materials.[11]

This article describes the nuclear physics platform on the OMEGA EP Laser System.[12] The following sections present the detectors used to characterize the ion flow from the converter target and to measure the neutron spectrum from nuclear interactions in the secondary targets; summarize the results from the first set of experiments using this platform; give the status of the analysis tools; and summarize the material.

Detectors

1. Thomson Parabola Ion Energy Analyzer

The energy spectrum of the ions was measured with a high-resolution Thomson parabola ion energy (TPIE) analyzer developed by a group from Los Alamos National Laboratory (LANL) for OMEGA EP[13] (see Fig. 156.15). The TPIE analyzer uses a 10-cm-long permanent magnet with a 5-kG magnetic field. The magnet is encased in an iron yoke with a 0.5-cm gap. A pair of 20-cm-long electrodes spaced 1 cm apart generate an electric field of up to 25 kV/cm. These electrodes are placed 1 cm behind the magnet.

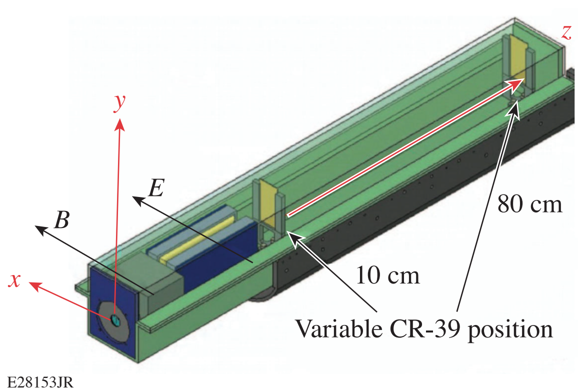

Figure 156.15
CAD model of the Thomson parabola ion energy (TPIE) analyzer from Ref. 13. The magnet is placed behind a pinhole, which is the origin of the coordinate system. The electric-field region is behind the magnet. Two possible detector locations are shown.

The magnetic field deflects positive ions upward (positive y direction); the electric field deflects them to the left (positive x direction). A pinhole of 100-μm or 250-μm diameter is mounted upstream of the magnet (origin of the coordinate system) and defines the solid angle of the instrument. The ions are recorded on either an image plate (IP)[14] or CR-39 track detector,[15] which can be mounted in three positions in the drift region: 10 cm, 50 cm, and 80 cm from the pinhole. This very versatile instrument can be used to discriminate between ions of different charge/mass ratios, for kinetic energies up to 150 MeV/u. The TPIE analyzer was absolutely calibrated using CR-39 track detectors, which have essentially a 100% detection efficiency for ions up to several tens of MeV. The IP was cross calibrated against the CR-39. Figure 156.16 shows a typical IP image from a shot with a deuterated plastic (CD) primary target. Hard x rays penetrating the filters and the pinhole produce a circular spot; the ions are deflected by the magnetic and electric fields and are recorded on parabolic-shaped curves. The two curves on the image correspond to protons, predominantly from contamination on the target surface, and deuterons from the target material.

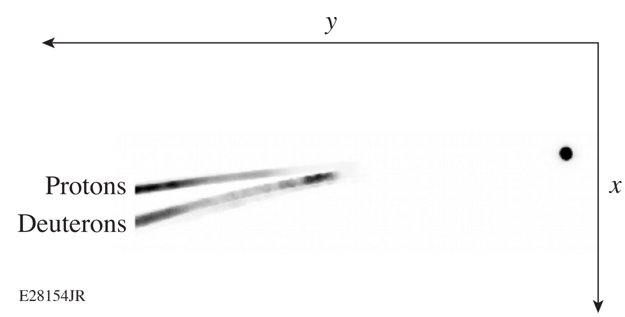

Figure 156.16
IP image from shot 19272 with a deuterated plastic (CD) primary target. The circular spot is caused by x rays passing through the pinhole. The ions are deflected by the magnetic (in the y direction) and electric (in the x direction) fields and are recorded on parabolic curves. The two curves on the image correspond to protons and deuterons, respectively.

2. Radiochromic Film

The divergence of the ion emission from the rear of the primary target was measured using a radiochromic film (RCF) stack.[16] Each stack contains a number of Al layers interleaved with RCF. RCF consists of one or more active dye layers coated on thin, transparent polyester substrates. When exposed to radiation, the active component undergoes a solid-state polymerization reaction, producing a color change from transparent to cyan blue or green, depending on the type of film. The depth of color change is proportional to the energy absorbed in the dye layer. Table 156.II describes the detailed configuration of the detector stack used in this study.

Table 156.II: Composition of the radiochromic film (RCF) stack.

Layer	Material	Label
1	100 μm Al	
2	HD-V2 film	H1
3	100 μm Al	
4	HD-V2 film	H2
5	100 μm Al	
6	HD-V2 film	H3
7	100 μm Al	
8	HD-V2 film	H4
9	500 μm Al	
10	MD-v2-55 film	M5

Two different RCF films were used: GafChromic HD-V2 (Ref. 17) with a single 12-μm active layer and a 97-μm polyester backing for the first four layers; and GafChromic MD-V2-55 (Ref. 18) with two 17.5-μm active layers and a total thickness of 283 μm for the fifth layer.

The Al layers in the stack slow down the incoming ions. Since the energy density deposited in the active layer in RCF films is much larger at the Bragg peak close to the end of the range of an ion of particular energy than at high energy, each film layer in the stack is energy selective to the ions with a range corresponding to the sum of the Al and film layers earlier in the path of an ion. The RCF and Al layers were cut into 6.5 × 6.5-cm^2 squares and placed 8 cm from the primary target in the target chamber.

Figure 156.17 shows examples of exposed RCF for shot 21763. A 20-μm-thick CH primary target was used for this shot with a laser pulse of 850 J, 10 ps focused to an 80 × 80-μm^2 spot, resulting in an intensity of ~1 × 10^{18} W/cm^2. Figure 156.17 shows (a) an image of the first film layer (H1) of the stack, which is most sensitive to protons of ~4-MeV energy, and (b) the fifth film layer (M5), which is sensitive to energies >15 MeV. The images show that the divergence is marginally higher at low energy (~45°) than at the higher energy (~30°).

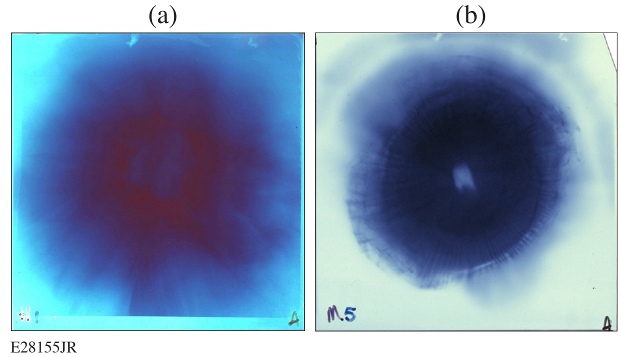

Figure 156.17
Radiochromic film (RCF) from (a) the first layer (H1) of the film stack and (b) the fifth layer (M5) of the stack for shot 21763. The H1 RCF is sensitive to protons of ~4-MeV energy, and the M5 layer is sensitive to energies >15 MeV.

3. Neutron Time-of-Flight Detectors

The detection of neutrons in short-pulse laser experiments is very challenging since it requires the neutron detection system to recover within 10 to 100 ns from a high background that is potentially many orders of magnitude stronger than the signal of interest. The background signal comes from the hard x-ray emission from the laser interaction with the target. A well-shielded nTOF detector with a plastic scintillator coupled with a photomultiplier tube (PMT) has been successfully used to measure neutrons in high-energy, short-pulse laser experiments with laser energies of up to 500 J (Ref. 19). At a higher laser energy of about 1 kJ at 10 ps, the x-ray shielding is ineffective since the shielding attenuation factor is approximately the same for x rays and neutrons.[20]

A promising method to suppress the background hard x-ray signal is to gate the PMT, rendering it inactive when the background signal is present. A microchannel-plate (MCP) PMT can be gated by applying a short positive pulse of the order of 200 V to the photocathode, which prevents the photoelectrons from reaching the MCP.[20] Gated PMT's still need to be shielded against hard x rays since these x rays will interact directly with the MCP, which is sensitive even when the photocathode is gated off. The direct interaction with the MCP could saturate the PMT and strongly reduce the system gain for the neutron signal. Additionally the light output from most scintillators has a significant component with a long decay-time constant, which produces a strong background once the PMT gate ends. This scintillator afterglow from the x-ray signal can mask neutron signals in short-pulse laser experiments. Therefore, a scintillator material with a significantly reduced long-decay component is required. A low-afterglow liquid scintillator described in the literature showed a >100× lower light output for times >100 ns after the primary event.[21] This liquid scintillator is based on a mixture of two dyes, PPO and bis-MSB, dissolved in xylene and saturated with oxygen. A neutron detector based on this liquid scintillator material has been developed for fast-ignitor experiments on OMEGA.[20]

A set of three gated liquid scintillator detectors was installed on OMEGA EP to measure the nTOF spectrum in three lines of sight (see Fig. 156.18). One detector was installed at ~45° from the laser's forward direction (north, Port 87) on the floor of the OMEGA EP Laser Bay near the concrete shield wall at 7.4 m from target chamber center (TCC). The second detector was mounted below the target area at ~90° from the laser direction at 8.4 m from TCC (down, Port 90), and the third detector was placed 15.1 m from TCC at ~150° with respect to the laser forward direction (south, Port 73). For all three detectors, the scintillator volume is shielded from hard x rays with ~2.5-cm lead plates in the direction to the target, and the detector PMT is shielded all around with ~10-cm-thick lead bricks. Since it is expected that more neutrons are generated into the laser forward direction, the volumes of the scintillator liquids are chosen to make the north detector the least sensitive using an ~0.5-L scintillator volume. The down detector uses an ~1-L volume, and the south detector is the most sensitive with an ~4-L scintillator volume. The gain of the PMT's in the three detectors is carefully adjusted to avoid saturation of the PMT and to minimize the digitizing noise from the oscilloscope recording.

Figure 156.19 shows a set of nTOF signals from the three liquid scintillator detectors recorded on shot 16076 with a CD primary and a CD secondary target at 1.2- kJ energy, 10-ps pulse duration, and 200-μm focal spot size. Even though the detectors are heavily shielded against x rays and gated off until

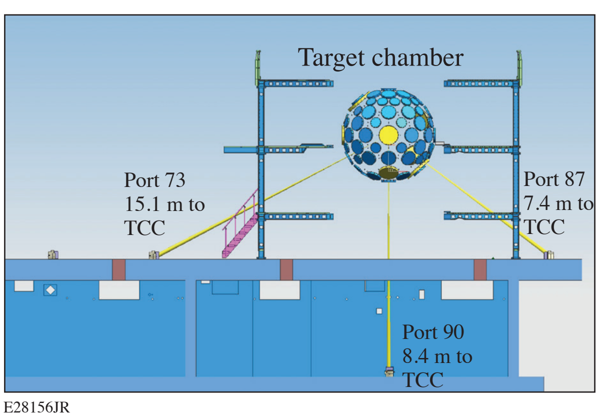

Figure 156.18
CAD model of the layout of the three neutron time-of-flight (nTOF) detectors on OMEGA EP located at different distances from target chamber center (TCC).

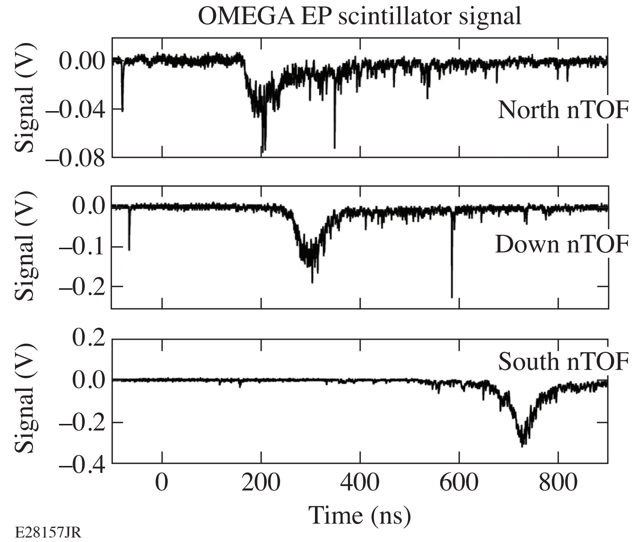

Figure 156.19
Signals from all three OMEGA EP nTOF detectors on a shot with a CD primary and CD secondary target at 1.25-kJ energy, 10-ps pulse duration, and 200-μm focal spot size (shot 16076).

50 to 100 ns after the laser interaction, a clear signature of the prompt x rays can be seen in both the north and down detectors as a spike at –70 ns. Since most of the x rays are emitted in the laser forward direction, the south detector records only a very small signal, which is not visible in Fig. 156.19. When the gate ends, a small remnant of the light decay from the prompt x-ray signal can be seen only in the north detector at ~ –20 ns since it sees the highest x-ray flux. The nTOF spectrum shows a significantly different shape in the three detectors determined by the TOF distance and the angular distribution of the neutron emission.

4. Neutron Activation Detector

A set of two nuclear activation sample holders was designed and built to provide additional information about the neutron spectrum. The nuclear activation samples are based on the activation of ^{152}Eu with thermal neutrons (see Fig. 156.20).

Europium is well suited as an activation material since it has a high cross section (1400 b) for thermal and epithermal neutrons populating an isomeric state that decays with a half-life of 9.3 h to ^{152}Sm, which facilitates handling and counting of the samples. The Eu samples are mounted in a high-density polyethylene (HDPE) sample holder, which acts as a moderator for the fast (2.5-MeV) neutrons expected for the reactions in the secondary targets. Two Cd filters are used to suppress background of scattered thermal neutrons (Fig. 156.21).

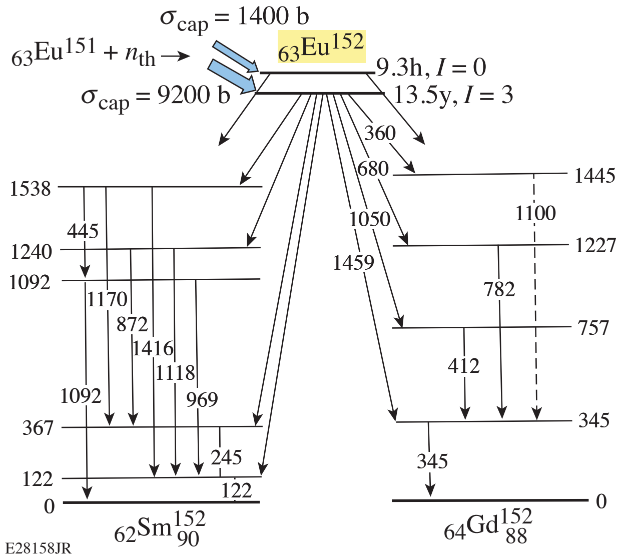

Figure 156.20
Nuclear energy level diagram of ^{152}Eu from Ref. 22.

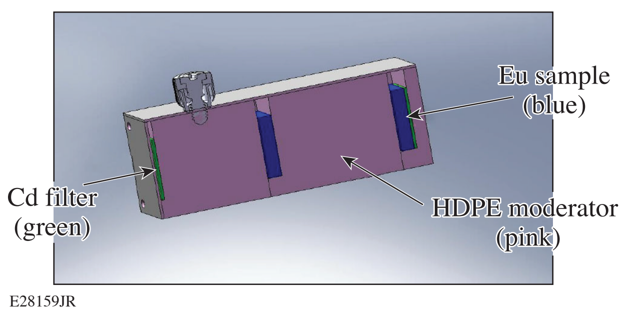

Figure 156.21
CAD model of the ^{152}Eu nuclear activation sample holder, showing the Cd filters, the Eu samples, and the high-density polyethylene (HDPE) moderator.

Experiments

1. Proton–Neutron Background Reduction

Excessive neutron background was seen in early experiments on the nTOF detectors. These shots used 200 × 200 × 20-μm^3 Cu foil primary targets, which were irradiated by a 10-ps pulse of 1.5-kJ energy, focused to an ~20-μm-radius spot, containing 80% of the laser energy for an average on-target laser intensity of ~10^{19} W/cm^2 [Fig. 156.22 (red curve)]. This background originates from (p,n) reactions of protons accelerated from the front and back sides of the primary targets interacting with the target chamber and diagnostics inserted into the target chamber.

To mitigate this issue, the primary target was redesigned to better confine the charged-particle flux toward only the secondary target and to minimize extraneous interactions. The redesigned primary target is housed in a 2-mm-long polystyrene (CH) tube with a 1.5-mm diameter. It is placed ~500 μm from the entrance of the tube (see Fig. 156.23). Since carbon has a high threshold for (p,n) reactions of >20 MeV, placing CH shields to intercept all protons that do not interact with the secondary target significantly reduces the background, provided that the proton spectrum does not contain a large number of protons above 20 MeV. A UV pulse was fired 0.5 ns ahead of the main laser pulse to generate a pre-plasma. It has

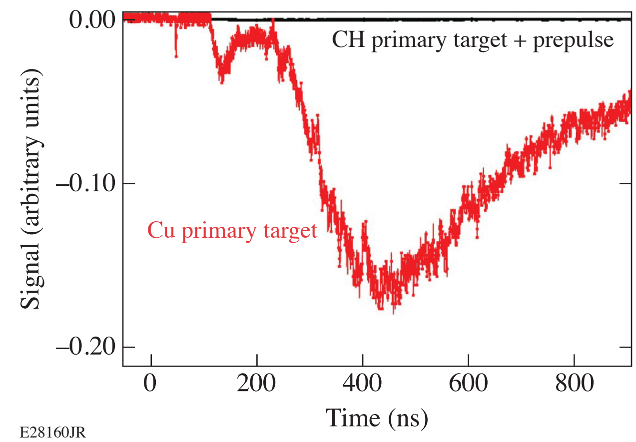

Figure 156.22
Neutron time-of-flight signal recorded by the OMEGA EP nTOF-south from a simple primary target configuration at ~10^{19} W/cm^2 (red curve) and the new CH primary target (black curve) at ~10^{18} W/cm^2, showing an ~100× reduction in background. The first peak seen at ~50 ns is a result of the x rays from the laser–target interaction; the second peak at ~120 ns is the light decay of the scintillator from the large x-ray peak after the gate turns off at ~100 ns.

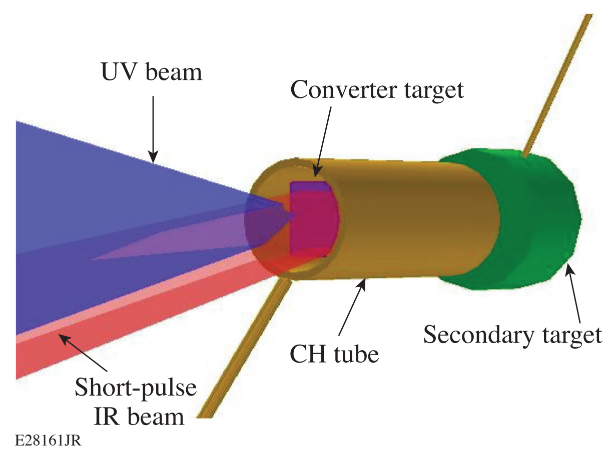

Figure 156.23
CAD model of the optimized converter target setup. The converter target is housed in a CH tube (gold cylinder), and the secondary target (green) is placed close to the end of the CH tube. A UV prepulse (red) is used to generate a pre-plasma before the high-intensity pulse (purple) arrives.

been shown in the literature that the longer density scale length associated with a pre-plasma significantly reduces the generation of fast ions.[23] The secondary target is also placed as close as possible to the primary target to intercept more of the solid angle, further reducing the proton flux, which could interact with material outside the targets. In addition, the laser intensity is reduced to below 10^{19} W/cm^2 by increasing the laser focal spot size to limit the maximum energy of the protons/deuterons to less than 20 MeV.

The black line in Fig. 156.22 shows data from the redesigned target configuration, using a $1000 \times 1000 \times 20$-$\mu$m^3 CH foil with a CH secondary target as shown in Fig. 156.23. A 100-ps, 100-J UV pulse was focused to strike the target 0.5 ns ahead of the main short pulse to generate a pre-plasma. The short pulse had a 10-ps pulse duration and 1.25 kJ of energy and was focused to an approximately square spot of ~80×80 μm^2, producing an average on-target laser intensity of ~10^{18} W/cm^2. A dramatic ~100× reduction in background was observed.

2. Characterization of the Ion Flow

To characterize the fast ion flow from the back side of the primary target, the energy distributions of the fast deuterons and protons from CD primary targets were measured in a separate shot (see Fig. 156.24), using the high-resolution TPIE analyzer (see **Thomson Parabola Ion Energy Analyzer**, p. 183). On this shot, the short-pulse laser delivered 400 J in 10 ps, focused to a square spot of ~80×80 μm^2 for an average on-target intensity of ~6×10^{17} W/cm^2. The target used in these experiments was of the same design as shown in Fig. 156.23, but with a CD foil as a converter target. No UV prepulse was used to mitigate the (p,n) background in this shot.

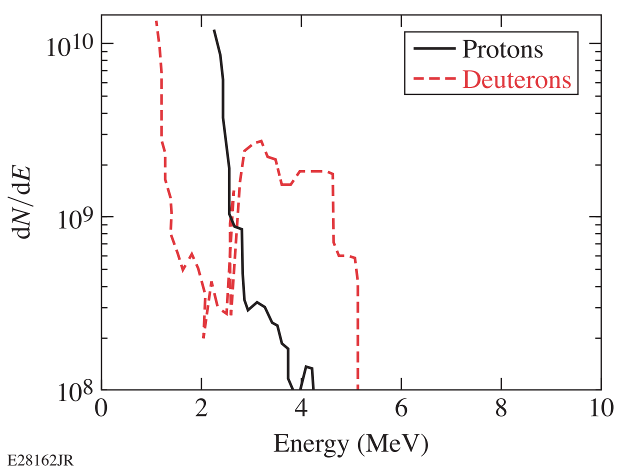

Figure 156.24
Ion spectra recorded by the TPIE analyzer for shot 19272.

The proton spectrum shows a typical exponential falloff with an end point at ~4 MeV. On the other hand, the deuteron spectrum exhibits a peak at 4±1 MeV. Surface contamination with water and hydrocarbons is most likely the source of the protons since the primary target contains very little hydrogen.

3. Proof-of-Principle Experiments with CD Targets

A first set of proof-of-principle experiments was conducted with CD primary and CD secondary targets to validate the nTOF setup using D–D nuclear fusion reactions. A $1000 \times 1000 \times 20$-$\mu$m^3 CD foil was irradiated by a 10-ps pulse of 1.25-kJ energy, focused to a square spot of ~100×100-μm^2 size. The average on-target laser intensity was ~1×10^{18} W/cm^2. A UV prepulse was used to minimize the (p,n) background. A secondary 2-mm-diam, 2-mm-thick CD target was placed 1 mm behind the primary target (see Fig. 156.23).

Figure 156.25 shows the neutron spectra from all three nTOF detectors from these experiments. Clear signatures of D–D fusion neutrons were observed in all three detectors. Kinematic shifts change the average energy of the detected neutrons in the forward (north) and backward (south) directions from the birth energy of 2.45 MeV to ~3.8 MeV and 1.8 MeV, respectively. At 90° from the flow of the primary deuterons, the average neutron energy is inferred to be ~2.5 MeV. The observed kinematic shifts are consistent with a mean energy of the deuteron flow of the order of ~1 MeV. The change in mean energy of the deuteron flow compared to the measurements shown in the previous subsection can be attributed to

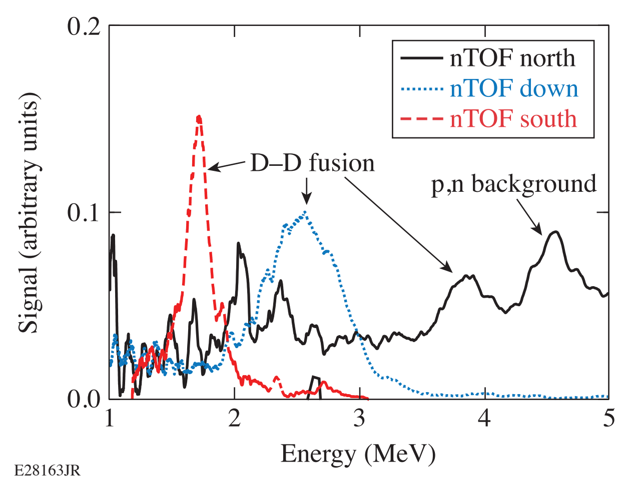

Figure 156.25
Neutron spectrum from all three OMEGA EP nTOF detectors on a shot with a CD primary and CD secondary target at 1.25-kJ energy, 10-ps pulse duration, and 200×200-μm^2 focal spot (shot 16076).

changes in the laser irradiation conditions, especially the use of a prepulse. The signal-to-background ratio is quite good for the south and down detectors; only in the north detector can a significant (p,n) background be observed. Using the calibration of the neutron detectors from OMEGA and accounting for the difference in attenuation from the changes in setup, a total neutron yield of ~2×10^8 can be inferred.

The Eu activation samples showed significant activation on these shots (see Fig. 156.26). The estimated neutron yield from the Eu cross section and the geometry of the setup is also of the order of ~2×10^8, which is consistent with the estimates from the nTOF detector.

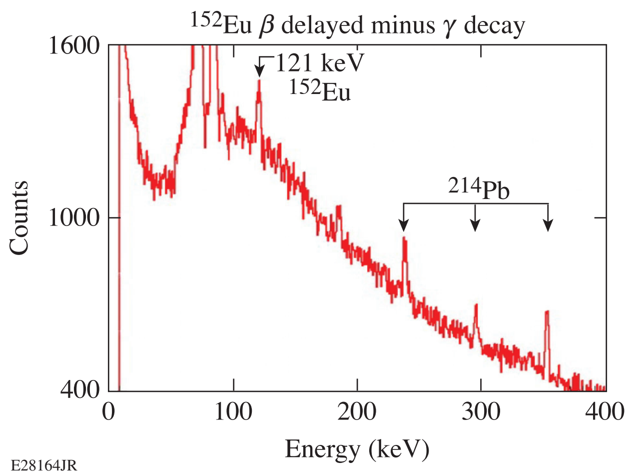

Figure 156.26
Gamma spectrum obtained from the ^{152}Eu samples exposed to the D–D fusion neutron flux. The lines attributed to ^{214}Pb are known background from the detector environment.

4. Experiments with Be Targets

A second set of experiments used Be secondary targets to explore the neutron generation in nuclear reactions of protons and deuterons with Be. Beryllium converters with thicknesses of 50 μm and 100 μm were placed on a CD secondary target, so that charged particles of sufficient energy, such as tritons generated in nuclear reactions with Be, could interact with the deuterons in the CD and potentially produce secondary neutrons.

Figure 156.27 shows the nTOF spectrum from the nTOF-south detector mounted ~150° from the laser's forward direction in experiments with and without the Be secondary target. A $1000 \times 1000 \times 20$-$\mu$m^3 primary CD target was irradiated by a 10-ps pulse of 1.25-kJ energy, focused to a ~100-μm-radius spot. The average on-target laser intensity was ~1×10^{18} W/cm^2. A secondary 2-mm-diam, 2-mm-thick Be/CD or CD target was placed 1 mm behind the primary target.

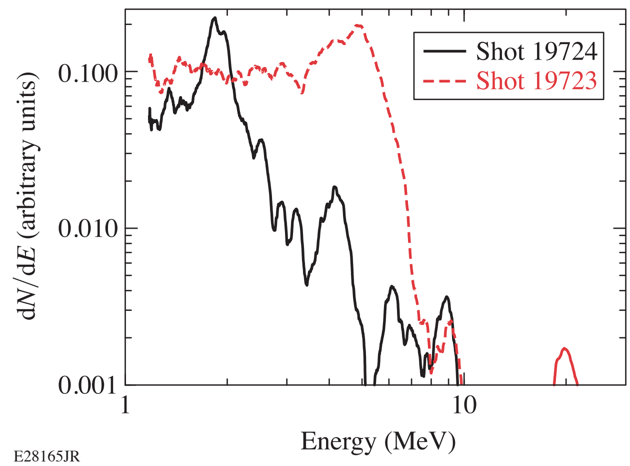

Figure 156.27
Neutron energy spectrum recorded by the nTOF-south detector for two consecutive shots, one with (19273) and one without (19274) the Be converter.

As expected, D–D fusion neutrons were observed for shot 19274 with the pure CD secondary. The observed kinematic shift and the total yield were identical to the measurements reported in **Proof-of-Principle Experiments with CD Targets** (p. 187).

A 50-μm Be foil was mounted in front of the CD target for shot 19273. The neutron spectrum changed significantly with the Be foil showing a prominent peak at ~5 MeV and a tail extending down to the detection limit of ~1 MeV. The neutrons at energies below ~4 MeV were most likely produced in ^{9}Be(d,n)^{10}B reactions.[24] This reaction has a maximum Q-value of ~4.4 MeV for the ground state of ^{10}B, which corresponds to ~4-MeV neutrons measured at the detector with the kinematic shift for an ~1-MeV deuteron taken into account. The resultant nucleus ^{10}B has a number of excited states, which can be populated in this reaction with probability similar to the ground state according to the literature.[24] The reactions into the first three excited states have Q-values of 3.6, 2.6, and 2.2 MeV, respectively. Neutrons emitted from these reactions can account for the tail going to a lower energy in the data. Very little data are available for the ^{9}Be(d,n)^{10}B reaction in the literature:[24,25] the published cross sections for a 1-MeV deuteron are typically of the order of 100 mb, comparable to the D–D fusion reaction cross section of ~200 mb at 1 MeV. There is no indication of secondary D–T fusion reactions, which would have resulted in a peak at ~12 MeV given the kinematics. A more-detailed analysis of the neutron spectrum from the Be reactions will be presented in **Comparison of Neutron Spectra with Accelerator Data** (p. 190).

5. Experiments with Layered CD/Be Converter Targets

To increase the sensitivity of the experiment to that of neutrons from potential secondary reactions, secondary targets with up to ten alternating layers of CD and Be with 25-μm thickness were introduced (see Fig. 156.28). The optimized setup of the primary CD foil target, as shown in Fig. 156.23, was retained. In these experiments the same UV prepulse as described in **Proton–Neutron Background Reduction** (p. 186) was used to suppress the (p,n) neutron background.

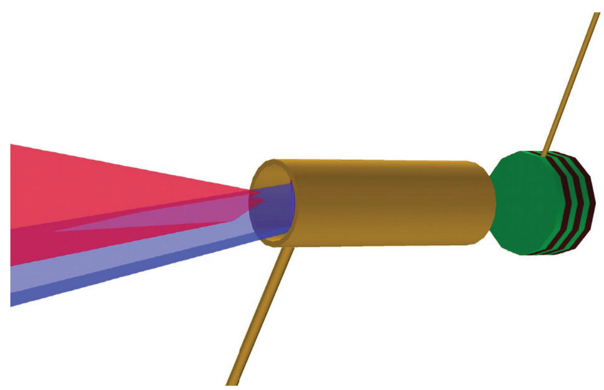

Figure 156.28
VISRAD model of the target setup with the layered secondary targets. Up to ten alternating layers of CD and Be with 25-μm thickness are used (only three layers of each are shown in the image).

Figure 156.29 shows neutron energy spectra from experiments with the layered secondary targets. The $1000 \times 1000 \times 20$-$\mu$m^3 primary CD target was irradiated by a 10-ps pulse of 1.25-kJ energy, focused to an ~100-μm-radius spot. The average on-target IR laser intensity was $\sim 1 \times 10^{18}$ W/cm^2. The 2-mm-diam secondary layered CD/Be target was placed 1 mm behind the primary target. Figure 156.29 shows the neutron energy spectra from the nTOF-south detector mounted ~150° from the laser's forward direction for two experiments: one where the fast ions interact with the CD layer first, and one where the target was rotated so that the ions interact with the Be layer first.

The D–D fusion neutron peak at ~1.8 MeV is more visible in the spectrum where ions interact with the CD first (black line) as compared to the spectrum where ions interact with Be first

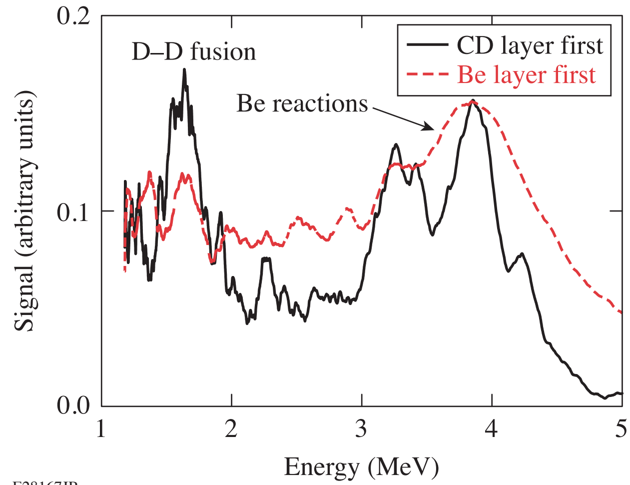

Figure 156.29
Neutron energy spectra from experiments with CD/Be layered secondary targets. Fast ions are either interacting with the CD layer first (black line, shot 21756) or with the Be layer first (red line, shot 21759).

(red line). This is consistent with the higher-energy loss of the ions in Be, where ~2-MeV deuterons have an estimated range of ~30 μm compared to a range of 50 μm in CD (Ref. 26).

The ^{9}Be(d,n)^{10}B reaction[24] peak at 3 to 4 MeV also changes with the composition of the first layer. The resultant ^{10}B nucleus has a number of excited states, which can be populated in this reaction with similar probability.[24] Therefore this complex feature is significantly broader than the D–D fusion neutron peak. There are indications of these excited states in the spectrum recorded with the CD layer in front of the Be layer. Because the cross section has a relatively sharp cutoff below 1 MeV and the deuterons lose significant energy in the CD layer, the resultant energy spread of the deuteron spectrum, which produces these neutrons, is much smaller compared to the case where the Be layer interacts first with the ion flow. The smaller energy spread of the deuteron spectrum leads to better-defined features for the different excited states.

The neutron signal for the Be reaction is a factor of ~4 to 5 higher than the neutron signal from the D–D fusion reaction. This is consistent with the ~2× higher abundance of Be, the 2× higher energy of the recorded neutrons, and the ~2× higher number density of Be. Further analysis is presented in **Simulations and Analysis** (p. 190).

Again in these experiments there is no indication of a D–T fusion reaction neutron peak that can be attributed to secondary neutrons, from either the tritons produced in one branch of the D–D fusion reaction or the ^{9}Be(d,t)^{8}Be pickup reaction. Such a D–T peak should have been recorded at ~12 MeV given the kinematics of the reaction.

Simulation and Analysis

1. Comparison of Neutron Spectra with Accelerator Data

The direct stripping reaction ^{9}Be(d,n)^{10}B was chosen for a suitable demonstration experiment at low deuteron energy since measurements have been performed in conventional experimental setups at an accelerator laboratory. Experimental double-differential neutron cross sections $d^2\sigma/\mathrm{d}\Omega \mathrm{d}E$ are available for this reaction at four different deuteron energies, ranging from 1.1 to 3.2 MeV. The reaction is exoenergic, with a Q-value of +4.36 MeV. Neutron transitions to the ground and several excited states in the final nucleus ^{10}B have also been characterized. In the experiment the secondary target was a stack of 25-μm-thick layers of ^{9}Be, alternating with thin layers of CD. The purpose of the latter component was to identify additional ^{9}Be + d reaction channels that emit deuterons or tritons through secondary D–T fusion reactions. The laboratory neutron energy spectra obtained in this experiment at the neutron detection angles θ_{lab} = 90° and θ_{lab} = 150° are displayed as symbols in Fig. 156.30. Line structure is clearly observable in either of the spectra, changing with detection angle in the expected fashion. Even though the deuteron beam had a continuous energy spectrum, this observation implies that the deuteron beam had a relatively well defined, mean kinetic energy. Exploiting the intrinsic calibration inherent in the data, this turns out to amount to $\langle E_{\mathrm{d}} \rangle \approx 0.9$ MeV. The actual width of the beam spectrum has not been determined independently in this experiment. This can be achieved, however, in future measurements using the available charged-particle diagnostics.

Figure 156.30 is also a comparison with computed neutron spectra based on published cross sections and kinematics (solid curves). In calculating the solid curves, the reported transition intensities to the final ^{10}B states were adopted for the two angles. A simplified description of the deuteron spectrum with a mean energy $\langle E_{\mathrm{d}} \rangle$ and standard width $\langle \sigma_{\mathrm{d}} \rangle$ was used, with the optimum values determined by a least squares fit. The peak energies of the D–D and ^{9}Be(d,n) neutrons, measured at two detection angles (90° and 150°), provided an internally consistent calibration for the energy and width of the deuteron spectrum. The calculated spectra agree quite well with the measurements, and the main structures in the two spectra and their angular variations are found to be compatible with the reported relative populations and the reaction kinematics.

2. Monte Carlo Simulations with *Geant4*

To be able to run realistic simulations of the OMEGA EP experiments, fusion cross sections based on the Bosch and Hale's parametrization[27] were added to the Monte Carlo particle transport framework *Geant4*.[28] The *Geant4* software package already includes primary and secondary particle tracking and physics modules to describe the slowing down of the incident ion flow in the secondary target as well as neutron scattering in the target and detector.

First tests show that the *Geant4* simulations correctly reproduce the relativistic kinematic of the in-flight D–D fusion reactions. Figure 156.31 compares the angular dependence of the

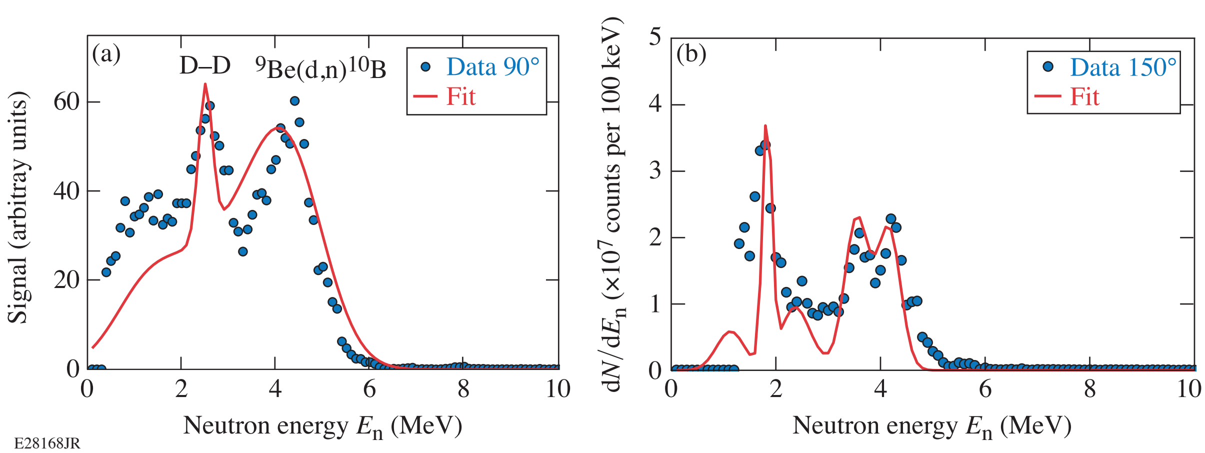

Figure 156.30
Energy spectra of neutrons from the ^{9}Be(d,n)^{10}B reaction at E_{d} = 0.9 MeV measured with nTOF detectors at (a) 90° and (b) 150° compared to modeled spectra (solid lines).

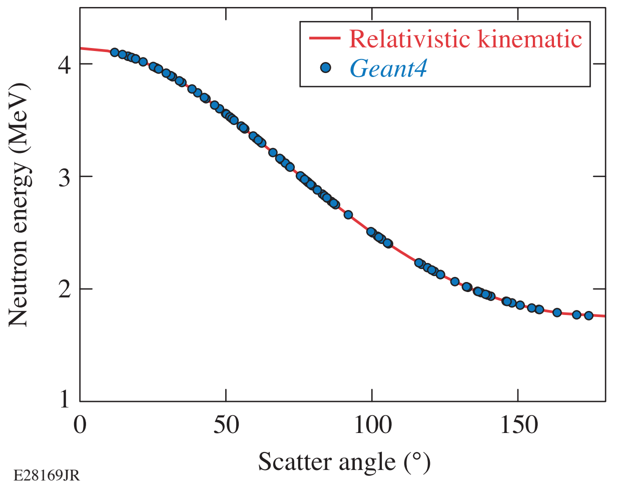

Figure 156.31
Neutron energy from fusion reactions as a function of scattering angle for a 1-MeV monoenergetic deuteron beam on a deuteron target. Relativistic kinematic calculations (red line) are compared to *Geant4* simulations using the newly implemented D–D fusion cross section.

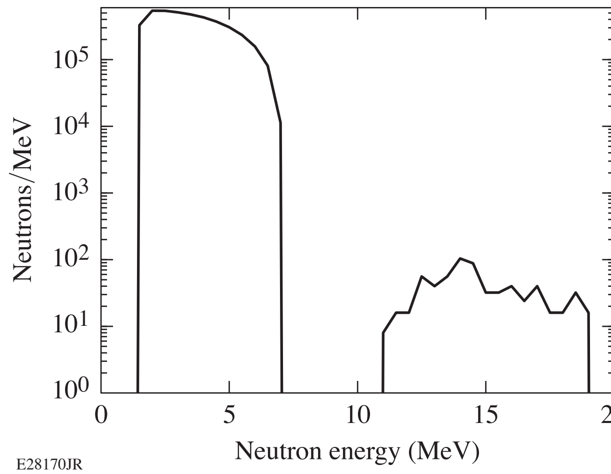

Figure 156.32
Neutron energy spectrum integrated over the full solid angle from a deuterium secondary target irradiated by a 4-MeV deuteron beam calculated by *Geant4*.

energy of the D–D fusion neutrons for a 1-MeV monoenergetic deuteron beam on a deuteron target predicted by relativistic kinematic calculations (red line) with corresponding *Geant4* simulations (blue symbols) using the newly implemented D–D fusion cross section. The *Geant4* simulated mean free path of the deuterons with respect to fusion reactions also agrees within a few percent compared to the values calculated directly from the cross section.

Figure 156.32 shows the calculated total neutron energy spectrum from a simulation using a 4-MeV deuteron beam impinging on a pure-deuterium target. A pure-deuterium target was chosen to improve the statistics. Nevertheless, the simulation took a few days on eight cores of a high-performance computing cluster. In this synthetical spectrum, neutrons from both the primary D–D fusion reaction (2 to 6 MeV) and the secondary D–T reaction (11 to 19 MeV) from the tritium produced in the d(d,t)p branch of the D–D reaction are visible. From the 8×10^9 incident primary particles, only about 0.1% produced a primary fusion neutron and about 0.1% of the tritons produced in the primary reactions generated a secondary neutron. As a result of the complex interaction between the energy loss of the fast ions (deuterons, tritons) in the target materials and because of the energy dependence of the fusion cross section, these conversion efficiencies are difficult to predict accurately without detailed simulations. Given that the dynamic range of our current detectors is ~100, these simulations indicate that it might not be feasible to detect secondary DT neutrons with the current detector system on OMEGA EP.

Summary

A setup to perform nuclear physics experiments on a high-energy, short-pulse laser system was presented. It is based on the principle of TNSA, where ions are liberated on the back side of a foil irradiated with a high-energy, short-pulse laser beam. The ions from the back side of the target are accelerated toward a secondary target in which they induce nuclear reactions.

The energy spectrum and species distribution of energetic ions from the primary target were characterized with a Thomson parabola. An RCF stack provided information about the divergence of the ion flow. Neutrons generated in nuclear reactions of the ions with the secondary targets were measured using an nTOF spectrometer with three detectors placed at 45°, 90°, and 150° from the direction of the ion flow. The absolute neutron yield was inferred with a neutron activation detector based on an Eu sample.

Two proof-of-principle experiments were performed with this setup. The first used a CD primary and CD secondary targets to generate D–D fusion neutrons, which provide a quasi-monoenergetic source of neutrons, and potentially secondary DT neutrons. Primary D–D fusion neutrons were detected with a signal to background of greater than 10, but no secondary DT neutrons were detected. The second experiment studied the stripping reaction ^{9}Be (d, n)^{10}B, which has a more-complicated neutron spectrum because of the presence of excited states in ^{10}B. After some optimization of the setup, discrete neutron spectral lines could be observed in the recorded nTOF signal. The measured neutron spectrum from the Be secondary target was compared against theoretical expectations and spectra measured on accelerators showing good correspondence. To be able to run realistic simulations of the complete setup for a more-detailed evaluation of the results, a project has been started to implement the relevant cross sections into the Monte Carlo transport code *Geant4*. As a first step, the D–D and D–T fusion cross sections were added and verified. First simulations of a D–D fusion setup showed that a dynamic range of four orders of magnitude on the detectors would be required to detect secondary DT neutrons.

This laser-based platform is especially useful for performing survey-type experiments of nuclear reactions since it provides a continuous ion spectrum. It can also be relatively easy to use rare or radioactive ions like tritium as projectiles or target nuclei since the interaction volume is quite small and easily confined in the target chamber.

ACKNOWLEDGMENT

This material is based upon work supported by the Department of Energy National Nuclear Security Administration under Award Number DE-NA0003856, the University of Rochester, and the New York State Energy Research and Development Authority.

REFERENCES

1. *Basic Research Needs for High Energy Density Laboratory Physics, Report of the Workshop on High Energy Density Laboratory Physics Research Needs*, Office of Science and National Nuclear Security Administration, U.S. Department of Energy, Washington, DC (15–18 November 2009).
2. C. J. Forrest, J. P. Knauer, W. U. Schroeder, V. Yu. Glebov, P. B. Radha, S. P. Regan, T. C. Sangster, M. Sickles, C. Stoeckl, and J. Szczepanski, Nucl. Instrum. Methods Phys. Res. A **888**, 169 (2018).
3. A. B. Zylstra, J. A. Frenje, M. Gatu Johnson, G. M. Hale, C. R. Brune, A. Bacher, D. T. Casey, C. K. Li, D. McNabb, M. Paris, R. D. Petrasso, T. C. Sangster, D. B. Sayre, and F. H. Séguin, Phys. Rev. Lett. **119**, 222701 (2017).
4. K. W. D. Ledingham, Nucl. Phys. A **752**, 633c (2005).
5. F. Hannachi *et al*., Plasma Phys. Control. Fusion **49**, B79 (2007).
6. S. C. Wilks *et al*., Phys. Plasmas **8**, 542 (2001).
7. M. S. Schollmeier, "Optimization and Control of Laser-Accelerated Proton Beams," Ph.D. thesis, Technische Universität Darmstadt (2008).
8. K. L. Lancaster, S. Karsch, H. Habara, F. N. Beg, E. L. Clark, R. Freeman, M. H. Key, J. A. King, R. Kodama, K. Krushelnick, K. W. D. Ledingham, P. McKenna, C. D. Murphy, P. A. Norreys, R. Stephens, C. Stoeckl, Y. Toyama, M. S. Wei, and M. Zepf, Phys. Plasmas **11**, 3404 (2004).
9. D. P. Higginson *et al*., Phys. Plasmas **17**, 100701 (2010).
10. S. Nakai *et al*., J. Phys.: Conf. Ser. **244**, 042027 (2010).
11. L. J. Perkins *et al*., Nucl. Fusion **40**, 1 (2000).
12. C. Stoeckl, J. A. Delettrez, J. H. Kelly, T. J. Kessler, B. E. Kruschwitz, S. J. Loucks, R. L. McCrory, D. D. Meyerhofer, D. N. Maywar, S. F. B. Morse, J. Myatt, A. L. Rigatti, L. J. Waxer, J. D. Zuegel, and R. B. Stephens, Fusion Sci. Technol. **49**, 367 (2006).
13. J. A. Cobble, K. A. Flippo, D. T. Offermann, F. E. Lopez, J. A. Oertel, D. Mastrosimone, S. A. Letzring, and N. Sinenian, Rev. Sci. Instrum. **82**, 113504 (2011).
14. C. C. Freeman, G. Fiksel, C. Stoeckl, N. Sinenian, M. J. Canfield, G. B. Graeper, A. T. Lombardo, C. R. Stillman, S. J. Padalino, C. Mileham, T. C. Sangster, and J. A. Frenje, Rev. Sci. Instrum. **82**, 073301 (2011).
15. N. Sinenian, M. J. Rosenberg, M. Manuel, S. C. McDuffee, D. T. Casey, A. B. Zylstra, H. G. Rinderknecht, M. Gatu Johnson, F. H. Séguin, J. A. Frenje, C. K. Li, and R. D. Petrasso, Rev. Sci. Instrum. **82**, 103303 (2011).
16. F. Nürnberg *et al*., Rev. Sci. Instrum. **80**, 033301 (2009).
17. GafChromic radiochromic film HD-V2, Ashland Advanced Materials, Bridgewater, NJ 08807, http://www.gafchromic.com/gafchromic-film/radiotherapy-films/HD-V2.
18. GafChromic radiochromic film MD-V2-55, GafChromic radiochromic film HD-V2, Ashland Advanced Materials, Bridgewater, NJ 08807, http://www.elimpex.com/new/products/radiation_therapy/Gafchromic/.
19. C. Stoeckl, V. Yu. Glebov, P. A. Jaanimagi, J. P. Knauer, D. D. Meyerhofer, T. C. Sangster, M. Storm, S. Sublett, W. Theobald, M. H. Key, A. J. MacKinnon, P. Patel, D. Neely, and P. A. Norreys, Rev. Sci. Instrum. **77**, 10F506 (2006).
20. C. Stoeckl, M. Cruz, V. Yu. Glebov, J. P. Knauer, R. Lauck, K. Marshall, C. Mileham, T. C. Sangster, and W. Theobald, Rev. Sci. Instrum. **81**, 10D302 (2010).
21. R. Lauck *et al*., IEEE Trans. Nucl. Sci. **56**, 989 (2009).
22. K. Debertin and R. G. Helmer, *Gamma- and X-Ray Spectrometry with Semiconductor Detectors* (North-Holland, Netherlands, 1988).
23. A. J. Mackinnon *et al*., Phys. Rev. Lett. **86**, 1769 (2001).
24. J. J. Devaney, Los Alamos National Laboratory, Los Alamos, NM, Report LA-4851, NTIS Document No. 197220 (1972).
25. R. A. Coombe and J. Walker, Proc. Phys. Soc. **80**, 1218 (1962).
26. J. F. Ziegler, M. D. Ziegler, and J. P. Biersack, Nucl. Instrum. Methods Phys. Res. B **268**, 1818 (2010).
27. H. S. Bosch and G. M. Hale, Nucl. Fusion **32**, 611 (1992).
28. J. Allison *et al*., Nucl. Instrum. Methods Phys. Res. A **835**, 186 (2016).